

Home Search Collections Journals About Contact us My IOPscience

Excitation dynamics in electrically asymmetric capacitively coupled radio frequency discharges: experiment, simulation, and model

This article has been downloaded from IOPscience. Please scroll down to see the full text article.

2010 Plasma Sources Sci. Technol. 19 045028

(http://iopscience.iop.org/0963-0252/19/4/045028)

View the table of contents for this issue, or go to the journal homepage for more

Download details:

IP Address: 134.147.180.34

The article was downloaded on 02/12/2010 at 16:29

Please note that terms and conditions apply.

Plasma Sources Sci. Technol. 19 (2010) 045028 (12pp)

# Excitation dynamics in electrically asymmetric capacitively coupled radio frequency discharges: experiment, simulation, and model

# J Schulze<sup>1,2</sup>, E Schüngel<sup>1</sup>, Z Donkó<sup>2</sup> and U Czarnetzki<sup>1</sup>

- <sup>1</sup> Institute for Plasma and Atomic Physics, Ruhr-University Bochum, Bochum, Germany
- <sup>2</sup> Research Institute for Solid State Physics and Optics of the Hungarian Academy of Science, Budapest, Hungary

E-mail: fjschulze@hotmail.com

Received 25 January 2010, in final form 9 June 2010 Published 23 July 2010 Online at stacks.iop.org/PSST/19/045028

#### Abstract

The symmetry of capacitively coupled radio frequency (CCRF) discharges can be controlled electrically by applying a fundamental frequency and its second harmonic with fixed but adjustable phase shift  $\theta$  between the driving voltages to one electrode. In such a discharge a variable dc self-bias  $\eta$  is generated as an almost linear function of  $\theta$  for  $0^{\circ} \le \theta \le 90^{\circ}$  via the Electrical Asymmetry Effect. The control parameter for  $\eta$  and the discharge symmetry is  $\theta$ . Here electron dynamics in electrically asymmetric geometrically symmetric dual frequency discharges operated in argon at 13.56 and 27.12 MHz is investigated experimentally by a particle-in-cell simulation and by an analytical model. The electron dynamics is probed by the electron impact excitation rate of energetic electrons from the ground state into highly excited levels. At high pressures (collisional sheaths) the excitation dynamics is found to work differently compared with conventional CCRF discharges. Unlike in classical discharges the maxima of the time modulated excitation at the powered and grounded electrode within one low frequency period will be similar (symmetric excitation), if  $\eta$  is strong at  $\theta \approx 0^{\circ}$ ,  $90^{\circ}$ , and significantly different (asymmetric excitation), if  $\eta \approx 0 \text{ V}$  at  $\theta \approx 45^{\circ}$ . At low pressures (collisionless sheaths) the excitation dynamics works similar to classical discharges, i.e. the excitation will be asymmetric, if  $\eta$  is strong, and symmetric, if  $\eta \approx 0$  V. This dynamics is understood in the frame of an analytical model, which provides a more detailed insight into electron heating in CCRF discharges and could be applied to other types of capacitive RF discharges as well.

(Some figures in this article are in colour only in the electronic version)

#### 1. Introduction

Capacitively coupled radio frequency (CCRF) discharges are frequently used for many applications such as etching and deposition processes used for semiconductor manufacturing [1,2]. For these applications separate control of ion energy and flux at the electrodes is essential. This separate control cannot be realized in single frequency discharges. Therefore, usually dual frequency discharges operated at two substantially different frequencies, e.g. 2 and 27 MHz, are used [3–7].

However, the coupling of both frequencies was found to limit the separate control of ion energy and flux in these discharges [8–15]. The Electrical Asymmetry Effect (EAE) allows us to control the ion energy separately from the ion flux in an almost ideal way in dual frequency discharges operated at a fundamental frequency and its second harmonic with fixed but adjustable phase shift  $\theta$  between the driving voltages [16–23]. Therefore, the EAE might be used as an alternative approach to realize this separate control in industry. In such electrically asymmetric discharges a dc self-bias  $\eta$  is generated as an almost

linear function of  $\theta$  for  $0^{\circ} \le \theta \le 90^{\circ}$  even in geometrically symmetric discharges. By tuning  $\theta$  the ion energy can be controlled by the variable dc self-bias without affecting the ion flux. Typically, the mean ion energy at the electrodes can be changed by a factor of about two by tuning  $\theta$  from  $0^{\circ}$  to  $90^{\circ}$ , while the ion flux remains constant within  $\pm 10\%$  [19, 20].

Electron heating and in particular stochastic heating in CCRF discharges are not fully understood and are important current research topics even in the case of simple single frequency discharges [24–34]. Studies of the space and phase resolved electron impact excitation rate of highly energetic electrons ( $E_{\rm e} \geqslant 10\,{\rm eV}$ ) from the ground state into high energy rare gas levels provided valuable insights into the mechanisms of electron heating in single as well as in classical dual frequency discharges [8–10, 33]. Here the term 'classical CCRF discharges' means CCRF discharges in which either no dc self-bias is generated or where the dc self-bias is generated geometrically and not electrically via the EAE. Excitation dynamics in electrically asymmetric discharges has not yet been investigated.

Experimentally the electron impact excitation rate from the ground state into specifically chosen energy levels can be calculated from phase resolved measurements of the emission resulting from transitions of electrons into lower energy states [35–37].

In this work excitation dynamics in electrically asymmetric geometrically symmetric dual frequency discharges operated in argon at 13.56 and 27.12 MHz is investigated for the first time experimentally by phase resolved optical emission spectroscopy (PROES), by a particle-in-cell (PIC) simulation and by an analytical model at different neutral gas pressures. High pressures of 60, 100 Pa and low pressures of about 3 Pa are chosen to investigate discharges with collisional (high pressure) and non-collisional sheaths (low pressure). It is found that depending on the pressure the excitation dynamics works differently in electrically asymmetric discharges compared with classical CCRF discharges. These differences are understood based on an analytical model, which in principle could be used to describe the excitation dynamics in other types of capacitive discharges as well.

The paper is structured in the following way: in the next section the experimental setup of the prototype of an electrically asymmetric geometrically symmetric discharge and the diagnostics used to investigate electron dynamics are described. In section 3 the basics of the PIC simulation used in this work are outlined. In section 4 the analytical model to describe and understand the excitation dynamics is introduced. Then the results are presented in section 5, which is divided into two parts: in the first part the excitation dynamics at high neutral gas pressures of 100 and 60 Pa (collisional sheaths) is analyzed and in the second part the excitation dynamics at low pressures of 2.66 Pa is investigated based on experimental, simulation and model results. Finally, conclusions are drawn in section 6.

## 2. Experimental setup

Here only a short outline of the experimental setup is given. A more detailed description can be found elsewhere [20]. Two

synchronized function generators (Agilent 33250A) are used to generate the phase locked 13.56 and 27.12 MHz voltage waveforms. The phase angle between these harmonics is adjusted via the frequency generators. Each voltage waveform is then amplified individually by a broadband amplifier and matched individually. Behind each matchbox a filter blocks the other harmonic. Behind the filters the two voltage waveforms are added and a voltage waveform  $\tilde{\phi}(t)$  of the following form is applied to the powered electrode:

$$\tilde{\phi}(t) = \tilde{\phi}_0(\cos(2\pi f t + \theta) + \cos(4\pi f t)). \tag{1}$$

Here  $f=13.56\,\mathrm{MHz}$ ,  $\theta$  is the phase angle between the applied voltage harmonics and  $\tilde{\phi}_0$  is the amplitude of one voltage harmonic. In the experiment the amplitudes of the two voltage waveforms are chosen to be identical in order to use similar conditions as in [17–19], although the EAE was demonstrated to be more effective at a particular choice of non-equal amplitudes [23].

The voltage drop across the discharge is measured by a LeCroy high voltage probe. A Fourier analysis of the measured voltage waveforms shows no significant generation of higher harmonic. The RF period average of the measured voltage yields the dc self-bias.

The radius of both electrodes (powered and grounded) The gap between the electrodes is  $d = 1 \,\mathrm{cm}$ . Both electrodes are located in a GEC cell [38]. The plasma is shielded from the outer grounded chamber walls by a glass cylinder. Therefore, the discharge is geometrically symmetric and the surface areas of the powered and grounded electrodes  $(A_{p/g})$  are identical. It is mainly operated in argon at low powers of a few watts. The presence of the glass cylinder causes an additional discharge asymmetry due to capacitive coupling between the cylinder and the outer grounded chamber wall. This capacitive coupling effectively enlarges the grounded surface area and causes an additional negative bias. As long as no discharge is ignited outside the cylinder this additional bias is less than 2% of the maximum bias generated electrically via the EAE and is, therefore, negligible. However, if a discharge is ignited between cylinder and outer chamber wall, which we avoided in the experiment, the additional bias will be stronger and no longer negligible. This restricts the set of discharge conditions, such as pressure and discharge gap, to a certain range, i.e. high neutral gas pressures cannot be used without decreasing the discharge gap. However, this would lead to an insufficient resolution of the optical measurements. The cylinder certainly also causes impurities in the plasma. However, these impurities are irrelevant for the qualitative investigations of excitation dynamics performed in this work.

In order to measure the emission from a specifically chosen neon state (Ne2p<sub>1</sub>) space and phase resolved 10% neon is admixed to the discharge. Besides other attributes the short lifetime of the Ne2p<sub>1</sub>-state makes this state particularly useful for PROES [37]. The emission at 585.5 nm is measured by an Andor Istar ICCD camera synchronized with the low frequency (lf) voltage waveform in combination with an interference filter. The temporal resolution of these measurements is 5 ns. Images are taken at different phases within the lf period (step

width of 5 ns). The resulting images are binned in horizontal direction and combined to an emission matrix providing onedimensional spatial resolution perpendicular to the electrodes of about 0.05 cm. From the emission the electron impact excitation rate from the ground state is calculated using a simple collisional-radiative model [35-37]. Measurements of the spatio-temporal excitation rate are performed at 60 Pa and  $\tilde{\phi}_0 = 76 \,\mathrm{V}$ . These conditions are similar, although not identical, to the high pressure conditions used in the simulation (100 Pa, 120 V). Higher pressures could not be realized experimentally due to the ignition of a discharge outside the glass cylinder at high pressures. To avoid damage of the frequency filters higher voltage amplitudes could not be used experimentally. Despite these differences between experiment and simulation the sheaths are collisional under both sets of conditions and the mean ion densities in the sheaths adjacent to the powered and grounded electrode are expected to be similar for all  $\theta$  in experiment and simulation, respectively. Based on the analytical model introduced in section 4, this is the only requirement that must be fulfilled to allow a qualitative comparison of the excitation dynamics in experiment and simulation. Measurements under conditions similar to the low pressure conditions used in the simulation (2.66 Pa, 315 V) are not discussed, since the spatio-temporal excitation could not be resolved in the experiment due to the limited temporal resolution and the small discharge gap. The excitation patterns originating from the top and bottom sheaths overlapped in the experiment.

# 3. PIC simulation

The simulation used in this work is a one-dimensional (1d3v) bounded plasma PIC simulation complemented with a Monte Carlo treatment of collision processes (PIC/MCC). At the planar, parallel and infinite electrodes, electrons are reflected with a probability of 20% [39] and the secondary electron coefficient is  $\gamma = 0.1$  [40]. The neutral gas temperature is taken to be  $T_{\rm g} = 350\,\rm K$ . The cross sections for electronneutral and ion-neutral collision processes are taken from [41–43]. The dc self-bias is determined in an iterative way by counting electrons and ions hitting each electrode within one If period and adjusting the bias iteratively to ensure that the charged particle fluxes to the two electrodes, averaged over one If period, balance. Details of the PIC simulation can be found elsewhere [14, 19, 44, 45].

The simulations are performed for two different neutral gas pressures of 100 Pa (collisional sheaths) and 2.66 Pa (non-collisional sheaths). In case of 100 Pa the electrode gap is 2 cm and in the case of 2.66 Pa it is 6.7 cm. The low pressure scenario, therefore, corresponds to conditions similar to the ones investigated experimentally by Godyak *et al* [46]. A voltage waveform given by equation (1) is applied to one electrode, while the other electrode is grounded. At 100 Pa  $\tilde{\phi}_0 = 120$  V and at 2.66 Pa  $\tilde{\phi}_0 = 315$  V is used. The excitation rate into a notionally lumped argon state is determined by counting individual excitation events. The cross section for excitation into this notionally lumped state is obtained by summing the cross sections for excitation into several argon

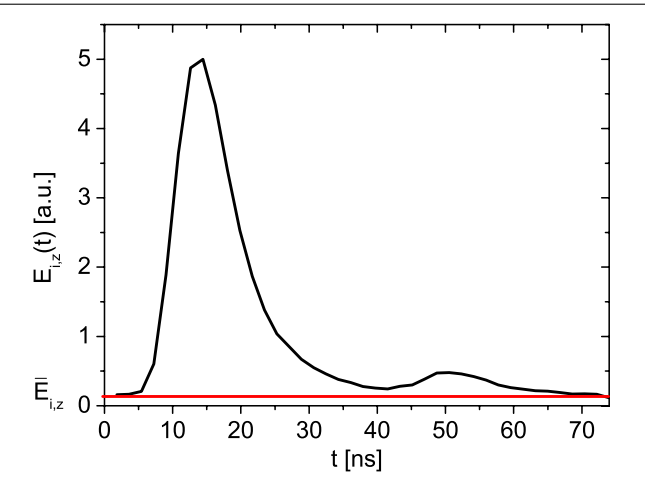


**Figure 1.** Total electron impact excitation rate at the position z indicated in figure 2 ( $\theta = 30^{\circ}$ ) by the horizontal line as a function of time (PIC). The horizontal line indicates the temporally constant fraction of the excitation  $\overline{E}_{i,z}$ .

levels [41]. In the following this excitation rate is called 'total excitation rate.'

# 4. Analytical model

The following analytical model is used to describe the dynamics of the time modulated fraction  $\widetilde{E}_{i,z}(t)$  of the total electron impact excitation rate from the ground state into a level i at a given position z close to the powered electrode (z=p) and close to the grounded electrode (z=g) at a time t within one If period. The ratio of  $\widetilde{E}_{i,p}(t_p)/\widetilde{E}_{i,g}(t_g)$  at two different times  $t_p$ ,  $t_g$  will be calculated from the applied RF voltage waveform and the symmetry parameter  $\varepsilon$  [17] for a geometrically symmetric discharge  $(A_p=A_g)$ .

$$\varepsilon = |\hat{\phi}_{s,g}|/|\hat{\phi}_{s,p}| \approx \bar{n}_{s,p}/\bar{n}_{s,g}. \tag{2}$$

Here  $|\hat{\phi}_{s,p}|$ ,  $|\hat{\phi}_{s,g}|$  are the maximum sheath voltages and  $\bar{n}_{s,p}$ ,  $\bar{n}_{s,g}$  are the spatially averaged ion density in the sheath adjacent to the powered and grounded electrode, respectively.

The electron impact excitation rate from the ground state into an excited level i at a position z and time t is generally given by

$$E_{i,z}(t) = \int_{v_{\text{ex}}}^{\infty} v^3 \sigma \langle f_z(v,t) \rangle_{\Omega} \, \mathrm{d}v. \tag{3}$$

Here v is the electron velocity,  $v_{\rm ex}$  is the electron velocity corresponding to the threshold for excitation into the observed level i,  $\sigma$  is the corresponding electron impact excitation cross section,  $f_z(v,t)$  is the electron velocity distribution function (EVDF) at the position z and time t and  $\langle f_z(v,t) \rangle_{\Omega} = \int f_z(v,t) \, \mathrm{d}\Omega$  is the integral of the distribution function over the full solid angle  $\Omega$ .

Generally, the total excitation can be split into a time independent part  $\overline{E}_{i,z}$  and a time dependent part  $\widetilde{E}_{i,z}(t)$ :

$$E_{i,z}(t) = \overline{E}_{i,z} + \widetilde{E}_{i,z}(t). \tag{4}$$

Figure 1 shows how the temporally constant and time modulated fractions of the total excitation rate at a given

position z and time t are determined practically. In this work only the maxima of the excitation adjacent to each electrode will be analyzed. First (as shown in figure 2 for  $\theta=30^\circ$  as an example), the spatial position z of a maximum of the total excitation rate close to one electrode is determined. A maximum close to the bottom electrode is chosen as an example. The spatial position z of this maximum is indicated by the horizontal line in figure  $2 \ (\theta=30^\circ)$ . Second (as shown in figure 1), the total excitation  $E_{i,z}(t)$  at this position z is plotted as a function of time. Third, the minimum excitation at this position z is identified with the temporally constant fraction of the total excitation at this position  $(\overline{E}_{i,z})$ . Finally,  $\widetilde{E}_{i,z}(t)$  is calculated from the difference between  $E_{i,z}(t)$  and  $\overline{E}_{i,z}$  at each time.

In a CCRF discharge operated at low neutral gas pressure the excitation is usually dominated by highly energetic electron beams generated by the expanding sheaths at both electrodes [16, 33, 47–50]. Therefore, the EVDF at a position z in the plasma bulk is non-local and assumed to be a superposition of an isotropic EVDF  $f_{\rm b}^{\rm c}(\vec{v})$  and the EVDF of the beam electrons:

$$f_z^{\text{beam}}(v,t) = \alpha_z f_{\text{b}z}^0(\vec{v} - \vec{u}_z(t)).$$
 (5)

By an analytical model such an assumption for the shape of the beam part of the distribution function has been demonstrated to reproduce time averaged Langmuir probe measurements in the plasma bulk (bi-Maxwellian distribution functions, [47]). Here  $\alpha_z = \bar{n}_{s,z}/n_{b,z}$  is the ratio of the mean ion densities in the respective sheath  $(\bar{n}_{s,z})$  and in the bulk  $(n_{b,z})$ . Typically  $\alpha_z \approx 0.1$ , i.e. the ion density in the sheath is one order of magnitude lower than in the plasma bulk. Consequently, the fraction of electrons, that are accelerated by the expanding sheath and form the beam, corresponds to 10% of the bulk density. Experimentally this value has been demonstrated to be realistic before [33].  $\vec{u}_z(t)$  is the drift velocity of the beam electrons. The beam EVDF is assumed to be  $f_{{\rm b},z}^0$  shifted by the drift velocity  $\vec{u}_z(t)$ . In order to avoid space charges the number of beam electrons that enter the bulk must equal the number of electrons that are removed from the isotropic part of the bulk EVDF. Thus, the EVDF in the plasma bulk  $f_{b,z}(\vec{v}, \vec{u}_z(t))$  is

$$f_{b,z}(\vec{v}, \vec{u}_z(t)) = f_{b,z}^0(\vec{v}) \cdot (1 - \alpha_z) + \alpha_z f_{b,z}^0(\vec{v} - \vec{u}_z(t)). \tag{6}$$

The flux density in the sheath is  $\bar{n}_{s,z}u_z$ . With the above velocity distribution the bulk flux density is conserved, i.e.  $u_{b,z}n_{b,z} = \bar{n}_{s,z}u_z$ .

Equation (6) can be expanded with respect to  $\vec{u}_z(t)$  around  $\vec{u}_z(t) = 0$  up to the second order to obtain [51]

$$f_{b,z}(\vec{v}, \vec{u}_z(t)) = f_{b,z}^0(\vec{v}) - \alpha_z(\vec{u}_z(t) \cdot \nabla_v) f_{b,z}^0(\vec{v}) + \frac{\alpha_z}{2} (\vec{u}_z(t) \cdot \nabla_v)^2 f_{b,z}^0(\vec{v}).$$
(7)

The dimensionless smallness parameter by which successive orders scale is  $u_z/v_{\rm th}$  with  $v_{\rm th}=\sqrt{2k_{\rm B}T_{\rm e}/m_{\rm e}}$  being the thermal electron velocity or an equivalent velocity for non-Maxwellian distributions. Expansion up to second order conserves the first three moments of the Boltzmann equation, i.e. density, velocity and energy.

Substitution of equation (7) into equation (3) yields the total excitation rate. Due to the averaging over the full solid angle all odd order terms in  $u_z$  vanish:

$$E_{i,z}(t) = \int \sigma v f_{b,z}^{0}(v) d^{3}v + \frac{\alpha_{z}}{2} u_{z}(t)^{2} \int \sigma v \frac{\partial^{2}}{\partial v_{z}^{2}} f_{b,z}^{0}(v) d^{3}v.$$
(8)

According to equation (4) the temporally constant and temporally modulated fractions of the total excitation are

$$\overline{E}_{i,z} = \int \sigma v f_{b,z}^{0}(v) \, d^{3}v = 4\pi \int_{v_{ex}}^{\infty} \sigma v^{3} f_{b,z}^{0}(v) \, dv, \tag{9}$$

$$\widetilde{E}_{i,z}(t) = \frac{\alpha_z}{2} u_z(t)^2 \int \sigma v \frac{\partial^2}{\partial v_z^2} f_{b,z}^0(v) d^3 v = \frac{\alpha_z}{2} u_z(t)^2 d_z.$$
(10)

Here

$$d_{z} = \int \sigma v \frac{\partial^{2}}{\partial v_{z}^{2}} f_{b,z}^{0}(v) d^{3}v$$

$$= \frac{4\pi}{3} \int_{v_{ex}}^{\infty} \sigma v \frac{\partial}{\partial v} \left( v^{2} \frac{\partial f_{b,z}^{0}(v)}{\partial v} \right) dv.$$
(11)

The ratio of the time modulated fraction of the excitation rate at a position z = p close to the powered electrode at time  $t_p$ ,  $\widetilde{E}_{i,p}(t_p)$ , and at a position z = g close to the grounded electrode at time  $t_g$ ,  $\widetilde{E}_{i,g}(t_g)$ , is then

$$\frac{\widetilde{E}_{i,p}(t_p)}{\widetilde{E}_{i,g}(t_g)} = \frac{\alpha_p}{\alpha_g} \cdot \frac{u_p(t_p)^2}{u_g(t_g)^2} \cdot \frac{d_p}{d_g}.$$
 (12)

Here  $t_p$  is the time within one If period, when maximum excitation at the powered electrode is observed.  $t_g$  is the time within one If period, when maximum excitation at the grounded electrode is observed. The electron conduction current density at times  $t_{p/g}$  is

$$j(t_{p/g}) = e\bar{n}_{s,p/g}u_{p/g}(t_{p/g}).$$
 (13)

Under the assumption that the displacement current in the plasma bulk is negligible, the conduction current densities are the same everywhere in the bulk and, thus, do not depend on z.

Substitution of equation (13) into equation (12) yields

$$\frac{\widetilde{E}_{i,p}(t_p)}{\widetilde{E}_{i,g}(t_g)} = \frac{\bar{n}_{s,g}}{\bar{n}_{s,p}} \frac{n_{b,g}}{n_{b,p}} \frac{d_p}{d_g} \left(\frac{j(t_p)}{j(t_g)}\right)^2 = \frac{1}{\varepsilon} \frac{n_{b,g}}{n_{b,p}} \frac{d_p}{d_g} \left(\frac{j(t_p)}{j(t_g)}\right)^2.$$
(14)

In a symmetric discharge  $n_{\rm b,g}/n_{\rm b,p}$  is unity. Generally, in an asymmetric discharge this factor can depend on  $\varepsilon$  (equation (2)). If  $n_{\rm b,g}/n_{\rm b,p} \approx \bar{n}_{\rm s,g}/\bar{n}_{\rm s,p}$  and  $d_{\rm g} \approx d_{\rm p}$  is assumed another factor  $1/\varepsilon$  results

$$\frac{\widetilde{E}_{i,p}(t_p)}{\widetilde{E}_{i,g}(t_g)} = \frac{1}{\varepsilon^2} \left( \frac{j(t_p)}{j(t_g)} \right)^2.$$
 (15)

The later approximation is based on the assumption that the unperturbed EVDF  $f_{\mathrm{b,z}}^0$  is the same on both sides of the discharge and, therefore,  $d_\mathrm{p} \approx d_\mathrm{g}$ .

Generally, a complicate dependence of  $n_{\rm b,g}/n_{\rm b,p}\cdot d_{\rm p}/d_{\rm g}$  on  $\varepsilon$  can exist. An expansion of this factor with respect to  $\varepsilon$  should have a leading power k. Considering only this leading power, i.e.  $n_{\rm b,g}/n_{\rm b,p}\cdot d_{\rm p}/d_{\rm g}\approx \varepsilon^{-k}$ , equation (14) has the form

$$\frac{\widetilde{E}_{i,p}(t_p)}{\widetilde{E}_{i,g}(t_g)} = \frac{1}{\varepsilon^{1+k}} \left( \frac{j(t_p)}{j(t_g)} \right)^2.$$
 (16)

Here k is a positive constant, that can depend on pressure and gas composition. In the case of  $\varepsilon \approx 1$  the total factor  $1/\varepsilon^{1+k}$  is close to unity, rather independent of k. Its value will be discussed in connection with the simulation results presented in the following section.

The ratio  $j(t_p)/j(t_g)$  is calculated from a global model of a CCRF discharge based on the voltage balance [52]:

$$\eta + \tilde{\phi} = -q^2 + \varepsilon'(q_t - q)^2. \tag{17}$$

Similar to [17] equation (17) is normalized to  $2\tilde{\phi}_0$ .  $\eta$ is the normalized dc self-bias, q is the normalized charge in the sheath adjacent to the powered electrode and  $q_t$  is the normalized total net charge in the discharge [17]. The charge-voltage relation of the sheath is assumed to be quadratic such as demonstrated experimentally and by a PIC simulation before [33,53]. The voltage drop across the plasma bulk is neglected, which has been proven earlier by PIC simulations for the neutral gas pressures investigated here [19].  $\varepsilon' = \varepsilon \frac{A_p}{A_a}$ is the symmetry parameter in its general form.  $\varepsilon'$  can be different from unity due to different mean ion densities in both sheaths, i.e.  $\varepsilon \neq 1$ , or due to different electrode surface areas or the combination of both. However,  $\varepsilon$  can only be different from unity due to different sheath densities. In the case of a geometrically symmetric discharge, such as discussed in this work, i.e.  $A_p = A_g$ ,  $\varepsilon' = \varepsilon$ .

Solving equation (17) for q yields

$$q(t) = \frac{-\varepsilon' q_{t} + \sqrt{\varepsilon' q_{t}^{2} - (1 - \varepsilon')(\eta + \tilde{\phi}(t))}}{1 - \varepsilon'}.$$
 (18)

Here  $q_t$  is assumed to be temporally constant [17,53]. Differentiation of q yields the conduction current density  $j(t) = Q_0\dot{q}(t)$ .  $Q_0$  is the normalization constant of q and  $q_t$  [17]:

$$j(t) = -\frac{Q_0}{2\sqrt{\varepsilon'}} \frac{\dot{\tilde{\phi}}(t)}{\sqrt{q_t^2 - \frac{1 - \varepsilon'}{\varepsilon'}(\tilde{\phi}(t) + \eta)}}.$$
 (19)

Under the assumption of  $q_t = 1$  [17] substitution of equation (19) into equation (16) yields

$$\frac{\widetilde{E}_{i,p}(t_{p})}{\widetilde{E}_{i,g}(t_{g})} = \frac{1}{\varepsilon^{1+k}} \left( \frac{\dot{\tilde{\phi}}(t_{p})}{\dot{\tilde{\phi}}(t_{g})} \right)^{2} \frac{1 - \frac{1 - \varepsilon'}{\varepsilon'} (\tilde{\phi}(t_{g}) + \eta)}{1 - \frac{1 - \varepsilon'}{\varepsilon'} (\tilde{\phi}(t_{p}) + \eta)}.$$
(20)

To a good approximation the last fraction on the RHS of equation (20) is unity, even if  $\varepsilon'$  is small. For  $\varepsilon'=1$  it is exactly unity:

$$\frac{\widetilde{E}_{i,p}(t_p)}{\widetilde{E}_{i,g}(t_g)} \approx \frac{1}{\varepsilon^{1+k}} \left( \frac{\dot{\tilde{\phi}}(t_p)}{\dot{\tilde{\phi}}(t_g)} \right)^2. \tag{21}$$

Under the assumption of  $n_{\rm b,g}/n_{\rm b,p} \approx \bar{n}_{\rm s,g}/\bar{n}_{\rm s,p}$  and  $d_{\rm p} \approx d_{\rm g}$  the ratio of the time modulated fraction of the total excitation rate is determined only by the symmetry parameter  $\varepsilon$  and the temporal derivative of the applied voltage waveform. Under these assumptions equation (21) is simply

$$\frac{\widetilde{E}_{i,p}(t_p)}{\widetilde{E}_{i,g}(t_g)} \approx \frac{1}{\varepsilon^2} \left( \frac{\dot{\tilde{\phi}}(t_p)}{\dot{\tilde{\phi}}(t_g)} \right)^2.$$
 (22)

Amongst others this model yields the result that the time modulated part of the total excitation rate is proportional to  $u_z^2$  (see equation (10)). This result agrees with the argument of Gans *et al* made for atmospheric pressure conditions, that the time modulated part of the excitation should depend on the dissipated power density per electron, i.e.  $\widetilde{E}_{i,z}(t) \propto (1/n) \, \mathrm{d}P/\,\mathrm{d}V$  [54]. Here P is the power dissipated to electrons and V is the volume. With  $\mathrm{d}P/\mathrm{d}V = jE$  and under the assumption that the electron current is determined by the local electric field, i.e.  $j = -\mathrm{en}u_z = \sigma E$  (high pressure), where E is the electric field and  $\sigma$  is the plasma conductivity:

$$\frac{1}{n}\frac{\mathrm{d}P}{\mathrm{d}V} \propto u_z^2. \tag{23}$$

Therefore, this model supports the hypothesis that the time modulated part of the excitation is proportional to the power density dissipated to electrons per electron. However, it must be pointed out that the above argument [54] is only valid at high pressure (strict locality), whereas the discharge conditions investigated in this work are clearly non-local (low pressure).

# 5. Results

# 5.1. Excitation dynamics at high neutral gas pressure (100 Pa/60 Pa)

First, excitations dynamics in a geometrically symmetric electrically asymmetric discharge operated at high neutral gas pressures of 100 Pa (PIC simulation) and 60 Pa (experiment) will be analyzed. Under these conditions the sheaths are collisional and the mean ion densities in both sheaths are identical to a good approximation at all phase angles  $\theta$  ( $\varepsilon \approx 1$ ).

Figure 2 shows spatio-temporal plots of the total excitation rate,  $E_{i,z}(t)$ , of argon atoms at 100 Pa,  $\tilde{\phi}_0 = 120 \text{ V}$  and d=2 cm at different phase angles  $\theta$  (0°, 30°, 60° and 90°) resulting from the PIC simulation.

The dc self-bias normalized by the amplitude of the applied voltage waveform,  $\bar{\eta}$ , and the symmetry parameter,  $\varepsilon$ , as a function of  $\theta$  are shown in figure 3 for the same discharge conditions. Due to the EAE the dc self-bias changes from about -20% to about +20% of the total amplitude of the applied voltage in an almost linear way as a function of  $\theta$  for  $0^{\circ} \leqslant \theta \leqslant 90^{\circ}$ . Analogical results are found experimentally [17–20].

Similar excitation dynamics is observed experimentally at a relatively high pressure of 60 Pa. Figure 4 shows spatiotemporal plots of the excitation into Ne2p<sub>1</sub> in an argon discharge with 10% neon admixture ( $\tilde{\phi}_0 = 76 \text{ V}$  and d = 1 cm) at different phase angles  $\theta$  (0°, 30°, 60° and 90°). The temporal

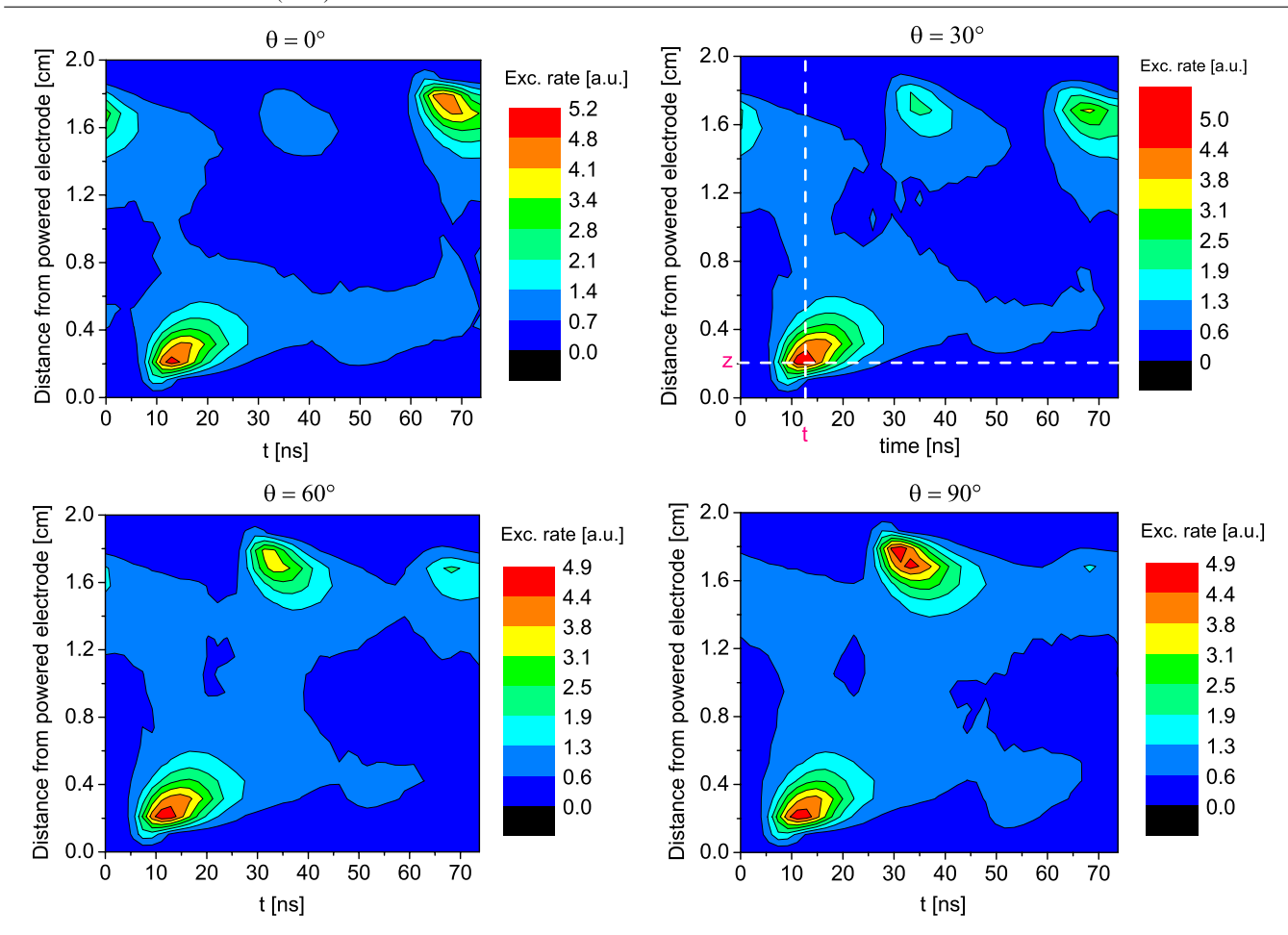
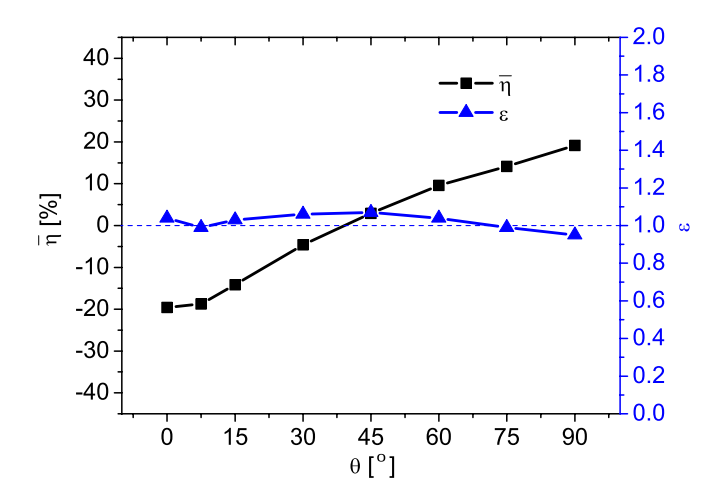


Figure 2. Spatio-temporal plots of the total excitation rate of argon atoms at 100 Pa,  $\tilde{\phi}_0 = 120$  V and d = 2 cm at different phase angles  $\theta$  (PIC simulation). In the case of  $\theta = 30^{\circ}$  the dashed lines indicate the time t (vertical line) and position z (horizontal line) of the excitation maximum adjacent to the powered electrode (see section 4).



**Figure 3.** Normalized dc self-bias and symmetry parameter as a function of  $\theta$  at 100 Pa,  $\tilde{\phi}_0 = 120$  V and d = 2 cm resulting from the PIC simulation.

resolution of these measurements is about 5 ns (camera gate width). Small differences to the simulation results shown in figure 2 might be explained by the lower pressure. In particular  $\varepsilon$  is not exactly unity for all  $\theta$  at 60 Pa. The effect of the symmetry parameter on the excitation dynamics will be discussed later.

Under these high pressure conditions the excitation dynamics exhibits unique attributes, which have not been observed in CCRF discharges before and which are in a sense oppositional to the excitation dynamics in classical CCRF discharges.

The excitation maxima observed in figures 2 and 4 are located at the edges of the sheaths adjacent to the powered and grounded electrode and are caused by the expansion of the respective sheath [33, 35, 36, 55]. Due to the change in the applied voltage waveform with  $\theta$  (see figure 5) the sheath dynamics and, consequently, also the excitation dynamics change as a function of  $\theta$ . At  $\theta = 0^{\circ}$  and  $\theta = 90^{\circ}$  the excitation maxima at the bottom and top electrodes are similarly strong, whereas at  $\theta = 30^{\circ}$  and  $\theta = 60^{\circ}$  the excitation maximum at the bottom electrode is significantly stronger than the maximum at the top electrode. In this sense the excitation is symmetric at  $0^{\circ}$  and  $90^{\circ}$  and asymmetric at  $30^{\circ}$  and  $60^{\circ}$ . Asymmetric excitation dynamics in geometrically symmetric, but electrically asymmetric has been predicted theoretically before [16, 17]. Here the spatio-temporal excitation profiles are only shown from  $0^{\circ}-90^{\circ}$  in  $30^{\circ}$ -steps. The strongest asymmetry of the excitation maxima at the top and bottom electrodes is found at  $45^{\circ}$  (figure 6). In the range  $90^{\circ}-180^{\circ}$  a similar change in the excitation dynamics as a function of  $\theta$  is

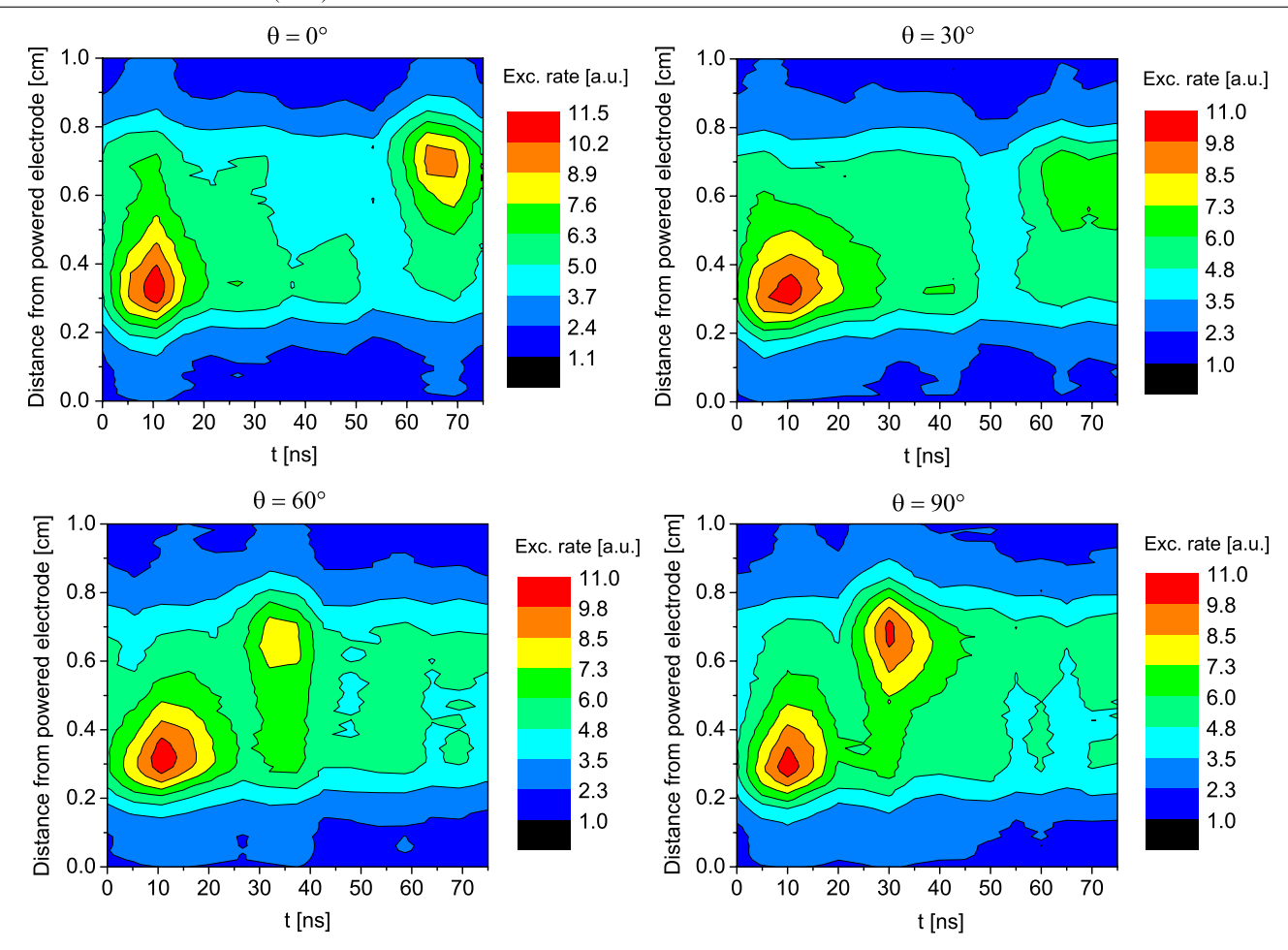
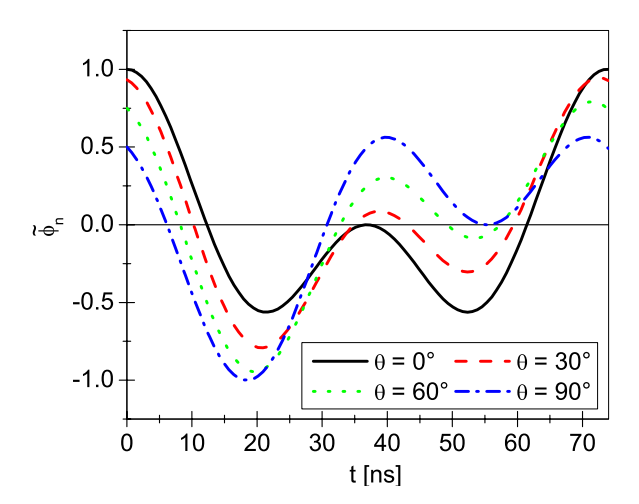


Figure 4. Measured spatio-temporal plots of the excitation rate into Ne2p<sub>1</sub> in an argon discharge with 10% neon admixture at 60 Pa,  $\tilde{\phi}_0 = 76 \text{ V}$  and d = 1 cm at different phase shifts  $\theta$ .



**Figure 5.** Applied voltage waveform normalized to its amplitude  $\tilde{\phi}_n$  as a function of time within one If period at different phase angles  $\theta$  (equation (1)).

observed, with the difference that the excitation maximum at the top electrode is stronger than the maximum at the bottom electrode.

At high pressures the strongest asymmetry of the excitation maxima is found around  $\theta = 45^{\circ}$ , i.e. at a phase angle of vanishing dc self-bias (see figure 3). The strongest

bias is generated around  $\theta = 0^{\circ}, 90^{\circ}$ . However, at these phase angles the excitation maxima at the top and bottom electrodes are similarly strong. This is substantially different to classical CCRF discharges operated at high pressures, in which the dc self-bias is generated by a geometric asymmetry (no EAE). In these discharges the asymmetry of the spatiotemporal excitation will be strongest, if the strongest dc selfbias is generated, which causes the maximum sheath voltages at both sides to become different. As a consequence of this, the sheath expansion velocity at one side will be decreased, while the expansion velocity on the other side will be increased. Here this is not the case: at high pressures the maximum sheath voltages are the same on both sides for all phase angles  $\theta$  $(\varepsilon = 1)$ , although the mean sheath voltages on both sides are different. Under these conditions the ion density profiles at both electrodes are the same and the sheath expansion velocities are determined only by the temporal change in the applied voltage waveform, which changes as a function of  $\theta$ (see figure 5).

This anomalous excitation dynamics is understood in the frame of the analytical model introduced in the previous section:

First, the time modulated fractions of the maxima of the total excitation rate at the powered and grounded electrode  $(\widetilde{E}_{i,p}(t_p), \ \widetilde{E}_{i,g}(t_g))$  at times  $t_p$ ,  $t_g$  are determined following

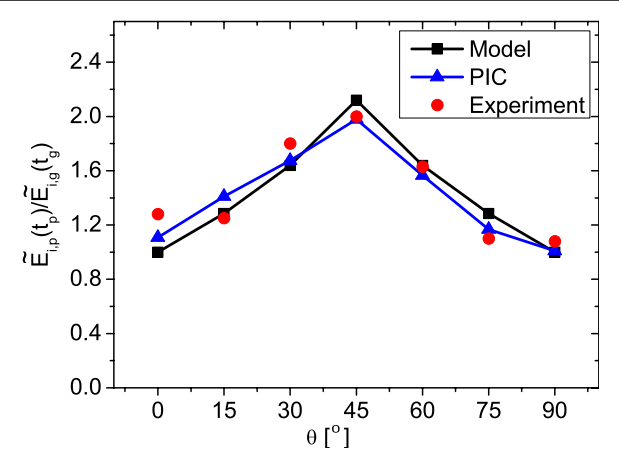


**Figure 6.** Ratio of the time modulated fraction of the excitation maxima close to the powered and grounded electrode resulting from the PIC simulation (figure 2, blue triangles and line) at 100 Pa, from the experiment (figure 4, red circles) at 60 Pa and from the analytical model (equation (24), black squares and line) assuming  $\varepsilon=1$  as a function of  $\theta$ .

the procedure described in section 4 (figure 1). In this way the ratio  $\widetilde{E}(t_p)_{i,p}/\widetilde{E}(t_g)_{i,g}$  of the time modulated fractions of the excitation maxima is obtained from the PIC simulation (figure 2) and from the experiment (figure 4) at different phase shifts  $\theta$ . Then this ratio is calculated by the analytical model using equation (22). At  $100 \, \text{Pa} \, \varepsilon \approx 1$  and only the temporal derivative of the applied voltage waveform is required as input parameter:

$$\frac{\widetilde{E}_{i,p}(t_p)}{\widetilde{E}_{i,g}(t_g)} \approx \left(\frac{\dot{\widetilde{\phi}}(t_p)}{\dot{\widetilde{\phi}}(t_g)}\right)^2. \tag{24}$$

Figure 6 shows the ratio of the time modulated part of the maxima of the total excitation rate,  $\widetilde{E}_{i,p}(t_p)/\widetilde{E}_{i,g}(t_g)$ , resulting from the PIC simulation (blue triangles and line, 100 Pa), the experiment (red circles, 60 Pa) and the analytical model (black squares and line,  $\varepsilon=1$ ). The excellent agreement between all three approaches demonstrates that the anomalous excitation dynamics under these high pressure conditions is caused by the mechanisms discussed above.

In addition to the correct prediction of the ratio of the time modulated fraction of the maxima of the total excitation rate at both electrodes, the phases within one If period, when the excitation maxima occur at each electrode can also be calculated by this model.

Using  $\varphi(t) = 2\pi f t$ ,  $\dot{\tilde{\phi}}(\varphi(t))$  is the first temporal derivative of the voltage waveform applied to the bottom electrode (equation (1)):

$$\dot{\tilde{\phi}}(\varphi(t)) = -\tilde{\phi}_0 2\pi f(\sin(\varphi + \theta) + 2\sin(2\varphi)). \tag{25}$$

The extrema of equation (25) are found at

$$\varphi_n = n\frac{\pi}{2} + \frac{\pi}{4} + \Delta n \tag{26}$$

with

$$\Delta n \approx \frac{\cos\left(n\frac{\pi}{2} + \frac{\pi}{4} + \theta\right)}{\sin\left(n\frac{\pi}{2} + \frac{\pi}{4} + \theta\right) + 8 \cdot (-1)^n}.$$
 (27)

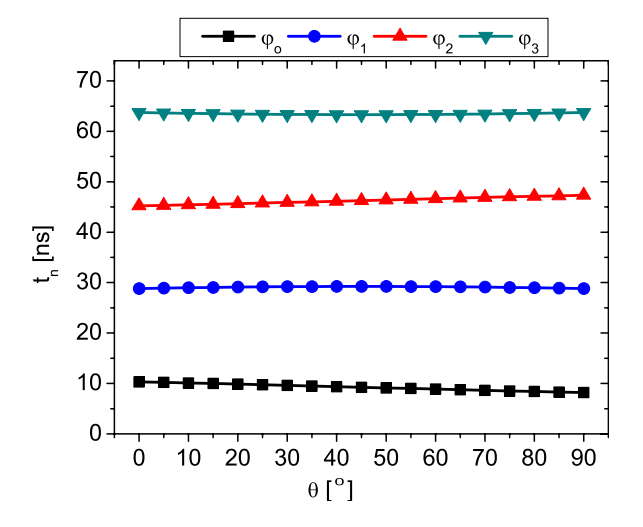


**Figure 7.** Times within one If period, when extrema of the first derivative of the applied voltage waveform occur (equation (28)) as a function of  $\theta$ .

Here n is a positive integer. Within one If period local extrema of the first derivative of the applied voltage waveform are found at the following four different phases  $\varphi_n$ :

$$\varphi_0 = \frac{\pi}{4} + \frac{1}{8} \cos\left(\frac{\pi}{4} + \theta\right) \approx \frac{\pi}{4},$$

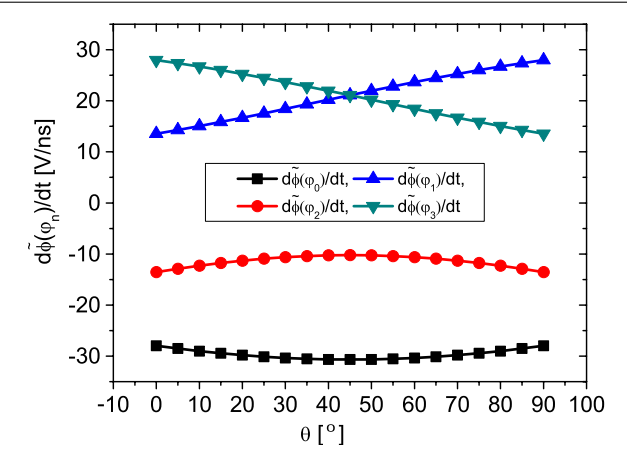
$$\varphi_1 = \frac{3\pi}{4} + \frac{1}{8} \sin\left(\frac{\pi}{4} + \theta\right) \approx \frac{3\pi}{4},$$

$$\varphi_2 = \frac{5\pi}{4} - \frac{1}{8} \cos\left(\frac{\pi}{4} + \theta\right) \approx \frac{5\pi}{4},$$

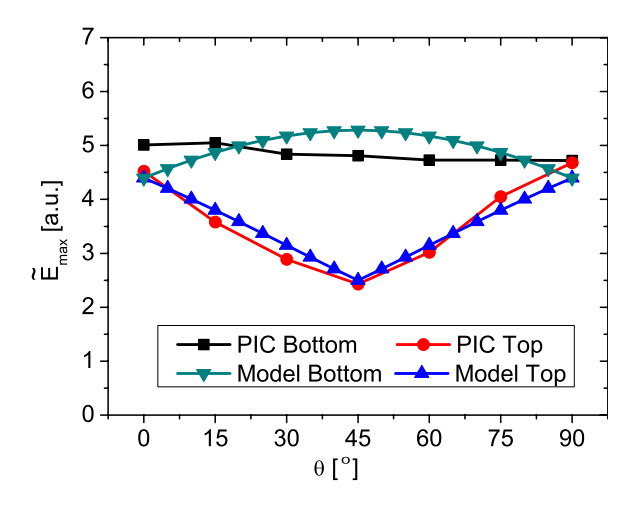
$$\varphi_3 = \frac{7\pi}{4} - \frac{1}{8} \sin\left(\frac{\pi}{4} + \theta\right) \approx \frac{7\pi}{4}.$$
(28)

Figure 7 shows the times within one If period, when extrema of the first derivative of the applied voltage waveform occur (equation (28)), as a function of  $\theta$ . According to equation (24) the maxima of the time modulated excitation are observed at these times. According to equation (28) the time when an individual extremum is found essentially does not change as a function of  $\theta$ . These times of maximum time modulated excitation predicted by the model (10, 29, 45 and 64 ns) agree well with the times of maximum excitation observed in the spatio-temporal excitation profiles resulting from the PIC simulation (11, 30, 47 and 66 ns, see figure 4) and the experiment (10, 31, 45 and 65 ns, see figure 6). In contrast to the phase, when an individual local extremum is found, the extremum itself and the time when the global extremum occurs do change.

Figure 8 shows the extrema of the first derivative of the applied voltage waveform as a function of  $\theta$ . Positive values, i.e.  $\dot{\tilde{\phi}}(\varphi_1)$  and  $\dot{\tilde{\phi}}(\varphi_3)$ , correspond to an expanding sheath at the grounded electrode, whereas negative values, i.e.  $\dot{\tilde{\phi}}(\varphi_0)$  and  $\dot{\tilde{\phi}}(\varphi_2)$ , correspond to an expanding sheath at the powered electrode [17]. Similar to the results of the simulation and the experiment the global minimum is  $\dot{\tilde{\phi}}(\varphi_0)$  for all  $\theta$ , i.e. strongest excitation at the powered electrode always happens at the same time  $t_p \approx 10$  ns within one If period for  $0^\circ \leqslant \theta \leqslant 90^\circ$ . Furthermore, the absolute value of this global minimum and,



**Figure 8.** Extrema of the first derivative of the applied voltage waveform as a function of  $\theta$ .



**Figure 9.** Maximum of the time modulated fraction of the total excitation rate at the bottom powered and top grounded electrodes as a function of  $\theta$  at 100 Pa resulting from the PIC simulation and the analytical model (PIC simulation data taken from figure 2, model data taken from figure 8 using equation (22)).

therefore, also the maximum excitation at the bottom electrode essentially do not change as a function of  $\theta$ . However, the global maximum of  $\tilde{\phi}(t)$  is found at different times within one If period depending on  $\theta$  and its absolute value does change as a function of  $\theta$ . At  $\theta=0^\circ$  and  $\theta=30^\circ$   $\tilde{\phi}(\varphi_3)$  corresponds to the global maximum and strongest excitation at the grounded electrode is observed at  $t_g\approx 65\,\mathrm{ns}$ . At  $\theta=60^\circ$  and  $\theta=90^\circ$   $\tilde{\phi}(\varphi_1)$  corresponds to the global maximum and strongest excitation at the grounded electrode is observed at  $t_g\approx 29\,\mathrm{ns}$ .

Figure 9 shows the maximum of the time modulated excitation at the bottom and top electrodes resulting from the PIC simulation and the analytical model at 100 Pa for  $0^{\circ} \le \theta \le 90^{\circ}$ . As predicted by the model, the maximum of the excitation at the bottom powered electrode is almost independent of  $\theta$ , whereas the maximum excitation at the top grounded electrode changes as a function of  $\theta$  with a minimum at  $\theta = 45^{\circ}$  and maxima at  $\theta = 0^{\circ}$ ,  $90^{\circ}$ . Similar results are found experimentally (see figure 10). Slight deviations between simulation/model data and the experimental results

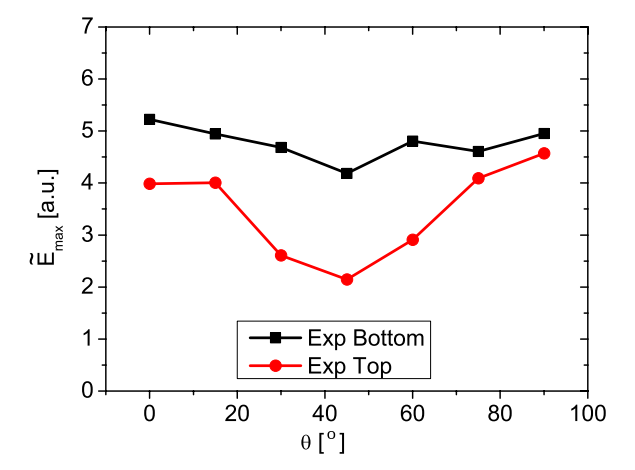


**Figure 10.** Maximum of the time modulated fraction of the total excitation rate at the bottom powered and top grounded electrodes as a function of  $\theta$  at 60 Pa resulting from the experiment (data taken from figure 4).

might again be explained by the lower pressure in the experiment. The analytical model reveals the physical reason for the observed change in the excitation maxima at the top and bottom electrodes as a function of  $\theta$ : based on equation (22) ( $\varepsilon=1$  at 100 Pa), the change in the temporal derivative of the applied voltage waveform as a function of  $\theta$  causes this characteristic. The temporal derivative of the applied voltage affects the sheath expansion velocity and, consequently, the drift velocity of the electron beams generated by the expanding sheath. Finally, this affects the excitation caused by the electron beams.

# 5.2. Excitation dynamics at low neutral gas pressure (2.66 Pa)

In this section excitations dynamics at low neutral gas pressure of 2.66 Pa will be analyzed, for which the sheaths are collisionless and the mean ion densities in both sheaths can be significantly different depending on the phase angle  $\theta$  ( $\varepsilon \neq 1$ ).

At these low pressures the excitation dynamics works substantially different compared with the high pressure scenario and similar to classical CCRF discharges. Figure 11 shows spatio-temporal plots of the total excitation rate of argon atoms at 2.66 Pa,  $\tilde{\phi}_0 = 315$  V and d = 6.7 cm at different phase angles  $\theta$  (0°, 30°, 60° and 90°) resulting from the PIC simulation. The normalized dc self-bias  $\bar{\eta}$  and the symmetry parameter  $\varepsilon$  as a function of  $\theta$  are shown in figure 12.

Again the excitation dynamics is dominated by sheath expansion heating. Due to the lower pressure and longer electron mean free path, the electron beams generated by the expanding sheaths propagate further into the plasma bulk. However, in contrast to high pressures the spatio-temporal excitation profiles are now asymmetric at  $\theta=0^\circ$  and  $\theta=90^\circ$  (symmetric excitation at high pressures) and almost symmetric at  $\theta=60^\circ$  (asymmetric excitation at high pressures).

At low pressures the ratio of the time modulated fractions of the maxima of the total excitation rates at both sides of the discharge,  $\widetilde{E}(t_p)_{i,p}/\widetilde{E}(t_g)_{i,g}$ , is no longer purely determined by the temporal derivative of the applied voltage waveform, since

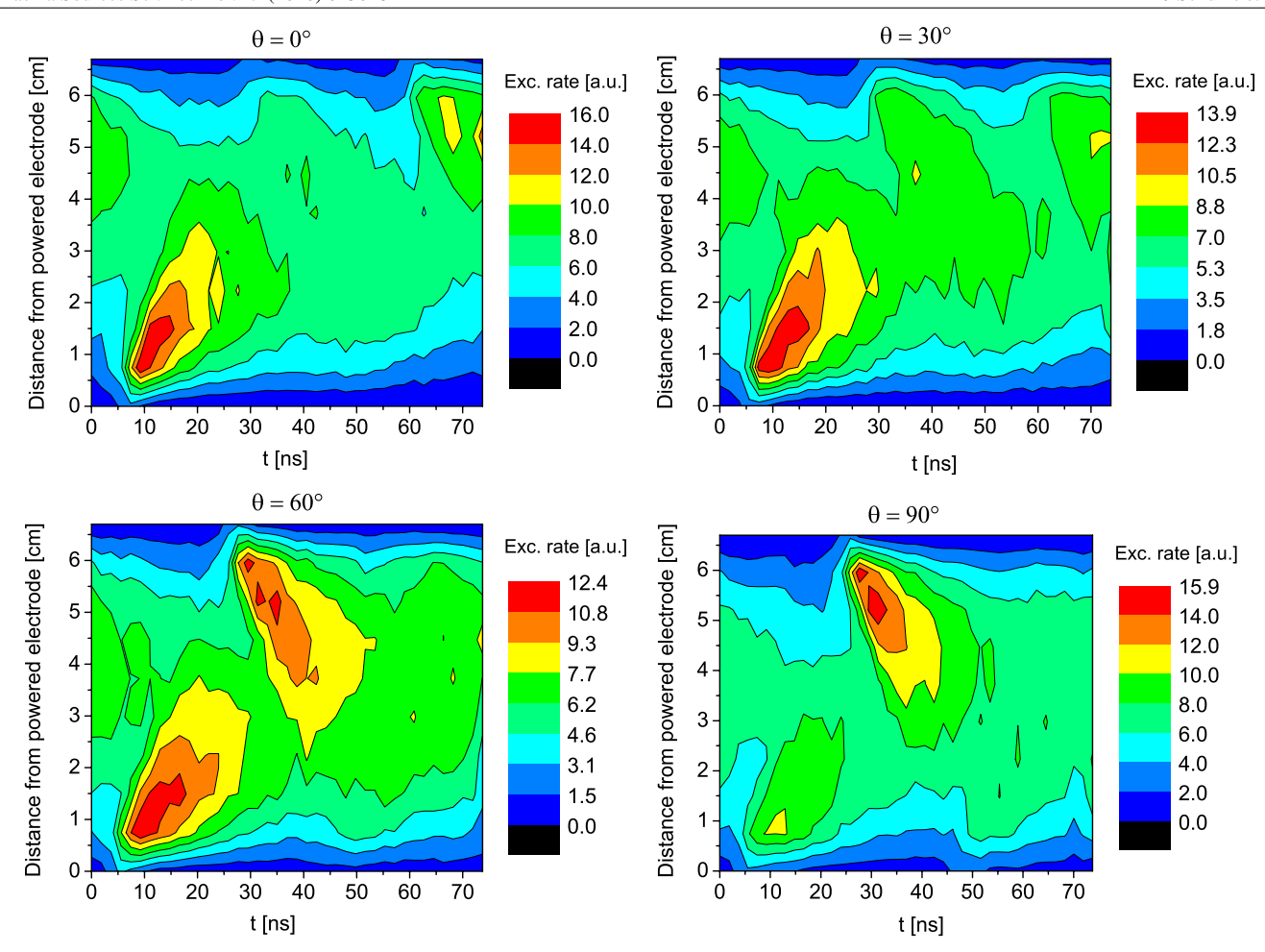
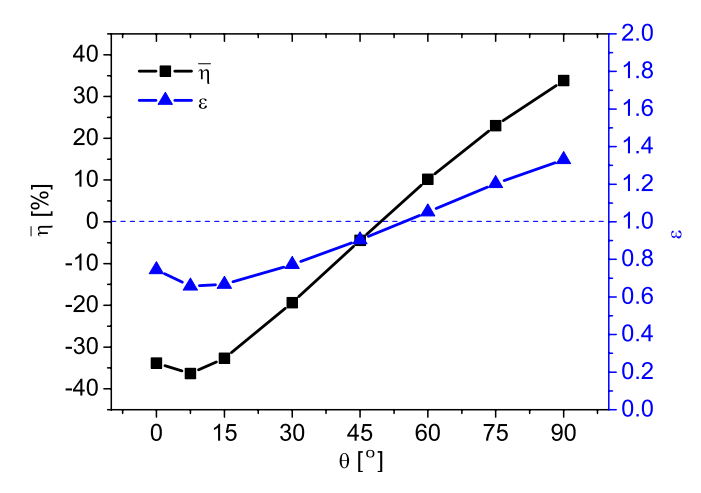
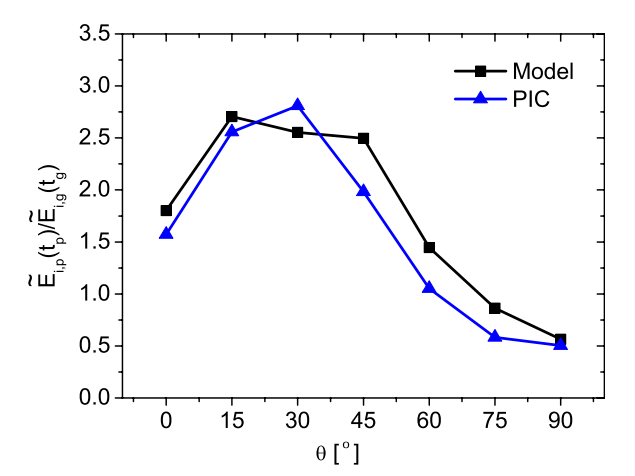


Figure 11. Spatio-temporal plots of the total excitation rate of argon atoms calculated by the PIC simulation at 2.66 Pa,  $\tilde{\phi}_0 = 315$  V and d = 6.7 cm at different phase angles  $\theta$ .



**Figure 12.** Normalized dc self-bias and symmetry parameter as a function of  $\theta$  at 2.66 Pa,  $\tilde{\phi}_0=315$  V and d=6.7 cm resulting from the PIC simulation.

the ion density profiles in the sheaths at both electrodes are no longer identical ( $\varepsilon \neq 1$ , figure 12, equation (22)). This is caused by the self-amplification of the EAE at low pressures [17–20]. A dc self-bias leads to different mean sheath voltages. Due to flux conservation at low pressures (collisionless sheath) a finite bias will lead to different mean ion densities in both



**Figure 13.** Ratio of the time modulated fraction of the total excitation maxima close to the powered and grounded electrode resulting from the PIC simulation (figure 11, blue triangles and line) and from the analytical model using equation (22) (black squares and line) as a function of  $\theta$  at 2.66 Pa.

sheaths. This causes the symmetry parameter to deviate from unity. Similar to the nature of the frequency coupling in dual frequency discharges operated at substantially different frequencies the sheath will expand faster, if the ion density at the position of the instantaneous sheath edge is lower [8–10]. For this reason, stronger excitation is observed adjacent to the sheath with the lower mean ion density. Furthermore, at low pressures the generation of a dc self-bias causes the maximum sheath voltages to be different. These mechanisms shift the phase angle  $\theta$  of strongest asymmetry of the spatio-temporal excitation profiles to phases of stronger dc self-bias, i.e. lower  $\theta$ , compared with the high pressure case.

This effect is reproduced by the analytical model using equation (22) with  $\varepsilon$  taken from the PIC simulation (figure 13). Due to the effect of the dc self-bias on the ion density profiles in both sheaths maximum asymmetry of the spatio-temporal excitation profiles is observed at lower  $\theta$  compared with the high pressure case. The good agreement between PIC and model results in figure 13 justifies the assumption made in the frame of the derivation of equation (22) in retrospect.

## 6. Conclusions

Spatio-temporal excitation dynamics in electrically asymmetric geometrically symmetric CCRF discharges driven at 13.56 and 27.12 MHz with fixed, but adjustable phase shift between the driving voltages has been investigated by a PIC simulation, an analytical model as well as experimentally at high (collisional sheaths) and low (collisionless sheaths) pressures. The excitation dynamics is found to be dominated by sheath expansion heating and to work substantially differently compared with classical CCRF discharges. Due to the collisionality of the sheaths at high pressures of 100 Pa the mean ion densities in both sheaths are identical ( $\varepsilon = 1$ ). Therefore, the symmetry of the spatio-temporal excitation is determined purely by the first derivative of the applied voltage waveforms at the times, when the excitation maxima at both electrodes are observed. Thus, unlike in classical CCRF discharges at high neutral gas pressures in a geometrically symmetric discharge driven at 13.56 and 27.12 MHz the spatio-temporal excitation is asymmetric at phase angles  $\theta$  of vanishing dc self-bias and symmetric at phase angles of strongest bias.

At low pressures (collisionless sheaths) the self-amplification of the EAE causes the mean ion densities in both sheaths and the maximum sheath voltages to be different at phase angles  $\theta$  of strong dc self-bias. This causes the sheaths of lower mean ion density to expand faster and, therefore, the spatio-temporal excitation to be asymmetric at phase angles of strong dc self-bias and symmetric at phase angles of vanishing bias. This excitation dynamics at low pressures in electrically asymmetric discharges is similar to the dynamics in classical CCRF discharges.

The analytical model introduced in this work describes the excitation dynamics in this particular type of electrically asymmetric CCRF discharge accurately and finally leads to an understanding of the electron dynamics. In principle this model should be applicable to describe electron dynamics in any kind of CCRF discharge and could, therefore, yield a more sophisticated understanding of excitation/ionization dynamics in other discharges as well.

# Acknowledgments

This work has been funded by the DFG through GRK 1051, the Ruhr-University Research Department Plasma, the Ruhr University Research School, the Alexander von Humboldt foundation and the Hungarian Scientific Research Fund through grant OTKA-K-77653.

# References

- [1] Lieberman M A and Lichtenberg A J 2005 Principles of Plasma Discharges and Materials Processing 2nd edn (New York: Wiley)
- [2] Makabe T and Petrovic Z 2006 Plasma Electronics: Applications in Microelectronic Device Fabrication (Boca Raton, FL: Taylor and Francis)
- [3] Boyle P C, Ellingboe A R and Turner M M 2004 *Plasma Sources Sci. Technol.* **13** 493–503
- [4] Boyle P C, Ellingboe A R and Turner M M 2004 J. Phys. D: Appl. Phys. 37 697
- [5] Kitajima T, Takeo Y, Petrovic Z L and Makabe T 2000 Appl. Phys. Lett. 77 489
- [6] Denda T, Miyoshi Y, Komukai Y, Goto T, Petrovic Z L and Makabe T 2004 J. Appl. Phys. 95 870
- [7] Lee J K, Manuilenko O V, Babaeva N Yu, Kim H C and Shon J W 2005 Plasma Sources Sci. Technol. 14 89
- [8] Gans T, Schulze J, O'Connell D, Czarnetzki U, Faulkner R, Ellingboe A R and Turner M M 2006 Appl. Phys. Lett. 89 261502
- [9] Schulze J, Gans T, O'Connell D, Czarnetzki U, Ellingboe A R and Turner M M 2007 J. Phys. D: Appl. Phys. 40 7008–18
- [10] Schulze J, Donkó Z, Luggenhölscher D and Czarnetzki U 2009 Plasma Sources Sci. Technol. 18 034011
- [11] Kawamura E, Lieberman M A and Lichtenberg A J 2006 Phys. Plasmas 13 053506
- [12] Turner M M and Chabert P 2006 Phys. Rev. Lett. 96 205001
- [13] O'Connell D, Gans T, Semmler E and Awakowicz P 2008 Appl. Phys. Lett. 93 081502
- [14] Donkó Z and Petrovic Z L 2006 Japan. J. Appl. Phys. Part 1 45 8151
- [15] Booth J P, Curley G, Marić D and Chabert P 2010 Plasma Sources Sci. Technol. 19 015005
- [16] Heil B G, Schulze J, Mussenbrock T, Brinkmann R P and Czarnetzki U 2008 IEEE Trans. Plasma Sci. 36 1404
- [17] Heil B G, Czarnetzki U, Brinkmann R P and Mussenbrock T 2008 J. Phys. D: Appl. Phys. 41 165202
- [18] Czarnetzki U, Heil B G, Schulze J, Donkó Z, Mussenbrock T and Brinkmann R P 2009 IOP Conf. Ser. 162 012010
- [19] Donkó Z, Schulze J, Heil B G and Czarnetzki U 2009 J. Phys. D: Appl. Phys. 42 025205
- [20] Schulze J, Schüngel E, Donkó Z and Czarnetzki U 2009 J. Phys. D: Appl. Phys. 42 092005
- [21] Donkó Z, Schulze J, Czarnetzki U and Luggenhölscher D 2009 Appl. Phys. Lett. 94 131501
- [22] Longo S and Diomede P 2009 Plasma Process. Polym. 6 370
- [23] Schulze J, Schüngel E, Donkó Z and Czarnetzki U 2009 J. Appl. Phys. 106 063307
- [24] Lieberman M A 1988 IEEE Trans. Plasma Sci. 16 638
- [25] Lieberman M A and Godyak V A 1998 *IEEE Trans. Plasma Sci.* **26** 955
- [26] Surendra M and Graves D B 1991 Phys. Rev. Lett. 66 1469
- [27] Turner M M 1995 Phys. Rev. Lett. 75 1312
- [28] Gozadinos G, Turner M M and Vender D 2001 Phys. Rev. Lett. 87 135004
- [29] Kaganovich I D 2002 Phys. Rev. Lett. 89 265006
- [30] Kaganovich I D, Polomarov O V and Theodosioue C E 2006 IEEE Trans. Plasma Sci. 34 696

- [31] Mussenbrock T, Brinkmann R P, Lieberman M A, Lichtenberg A J and Kawamura E 2008 Phys. Rev. Lett. 101 085004
- [32] Ziegler D, Mussenbrock T and Brinkmann R P 2008 Plasma Sources Sci. Technol. 17 045011
- [33] Schulze J, Heil B G, Luggenhölscher D, Brinkmann R P and Czarnetzki U 2008 J. Phys. D: Appl. Phys. 41 195212
- [34] Turner M M 2009 J. Phys. D: Appl. Phys. 42 194008
- [35] Gans T, Lin C C, Schulz-von der Gathen V and Döbele H F 2003 Phys. Rev. A 67 012707
- [36] Gans T, Schulz-von der Gathen V and Döbele H F 2004 Europhys. Lett. 66 232
- [37] Schulze J, Schüngel E, Donkó Z, Luggenhölscher D and Czarnetzki 2010 J. Phys. D: Appl. Phys. 43 124016
- [38] Miller P A, Hebner G A, Greenberg K E, Pochan P D and Aragon B P 1995 J. Res. Natl Inst. Stand. Technol. 100 427
- [39] Kollath R 1956 Encyclopedia of Physics vol XXI, ed S Flügge (Berlin: Springer) p 264
- [40] Böhm C and Perrin J 1993 Rev. Sci. Instrum. 64 31
- [41] Phelps A V and Petrović Z Lj 1999 Plasma Sources Sci. Technol. 8 R21
- [42] Phelps A V 1994 J. Appl. Phys. 76 747
- [43] Phelps A V http://jilawww.colorado.edu/~avp/collision\_data/ unpublished

- [44] Schulze J, Donkó Z, Heil B G, Luggenhölscher D, Mussenbrock T, Brinkmann R P and Czarnetzki U 2008 J. Phys. D: Appl. Phys. 41 105214
- [45] Donkó Z and Petrović Z Lj 2007 J. Phys.: Conf. Ser. 86 012011
- [46] Godyak V A, Piejak R B and Alexandrovich B M 1992 Plasma Sources Sci. Technol. 1 36
- [47] Schulze J, Heil B G, Luggenhölscher D, Czarnetzki U and Brinkmann R P 2008 J. Phys. D: Appl. Phys. (FTC) 41 042003
- [48] Schulze J, Heil B G, Luggenhölscher D and Czarnetzki U 2008 IEEE Trans. Plasma Sci. 36 1400
- [49] Vender D and Boswell R W 1992 J. Vac. Sci. Technol. A 10 1331
- [50] Wood B P 1991 PhD Thesis University of Berkeley, California
- [51] Crintea D L, Luggenhölscher D, Kadetov V A, Isenberg Ch and Czarnetzki U 2008 J. Phys. D: Appl. Phys. 41 082003
- [52] Czarnetzki U, Mussenbrock T and Brinkmann R P 2006 Phys. Plasmas 13 123503
- [53] Schulze J, Schüngel E, Donkó Z and Czarnetzki U 2010 J. Phys. D: Appl. Phys. 43 225201
- [54] Waskönig J and Gans T 2009 Bull. Am. Phys. Soc. BAPS.2009.GEC.FT1.4
- [55] Belenguer Ph and Boeuf J P 1990 Phys. Rev. A 41 4447